Video Article

High-throughput Measurement of Plasma Membrane Resealing Efficiency in Mammalian Cells

Jonathan G.T. Lam[1,2,3], Chi Song[4], Stephanie Seveau[1,2,3]

[1]Department of Microbial Infection and Immunity, The Ohio State University

[2]Department of Microbiology, The Ohio State University

[3]Infectious Diseases Institute, The Ohio State University

[4]Division of Biostatistics, College of Public Health, The Ohio State University

Correspondence to: Stephanie Seveau at Seveau.1@osu.edu

URL: https://www.jove.com/video/58351
DOI: doi:10.3791/58351

Keywords: Plasma membrane resealing, membrane repair, muscular dystrophy, propidium iodide, carbocyanine nucleic acid binding dye, pore-forming toxin, listeriolysin O

Date Published: 11/16/2018

Citation: Lam, J.G., Song, C., Seveau, S. High-throughput Measurement of Plasma Membrane Resealing Efficiency in Mammalian Cells. *J. Vis. Exp.* (), e58351, doi:10.3791/58351 (2018).

Abstract

In their physiological environment, mammalian cells are often subjected to mechanical and biochemical stresses that result in plasma membrane damage. In response to these damages, complex molecular machineries rapidly reseal the plasma membrane to restore its barrier function and maintain cell survival. Despite 60 years of research in this field, we still lack a thorough understanding of the cell resealing machinery. With the goal of identifying cellular components that control plasma membrane resealing or drugs that can improve resealing, we have developed a fluorescence-based high-throughput assay that measures the plasma membrane resealing efficiency in mammalian cells cultured in microplates. As a model system for plasma membrane damage, cells are exposed to the bacterial pore-forming toxin listeriolysin O (LLO), which forms large 30-50 nm diameter proteinaceous pores in cholesterol-containing membranes. The use of a temperature-controlled multi-mode microplate reader allows for rapid and sensitive spectrofluorometric measurements in combination with brightfield and fluorescence microscopy imaging of living cells. Kinetic analysis of the fluorescence intensity emitted by a membrane impermeant nucleic acid-binding fluorochrome reflects the extent of membrane wounding and resealing at the cell population level, allowing for the calculation of the cell resealing efficiency. Fluorescence microscopy imaging allows for the enumeration of cells, which constitutively express a fluorescent chimera of the nuclear protein histone 2B, in each well of the microplate to account for potential variations in their number and allows for eventual identification of distinct cell populations. This high-throughput assay is a powerful tool expected to expand our understanding of membrane repair mechanisms via screening for host genes or exogenously added compounds that control plasma membrane resealing.

Video Link

The video component of this article can be found at https://www.jove.com/video/58351/

Introduction

Mammalian cells are subject to mechanical, osmotic, and biochemical stress, resulting in the loss of plasma membrane integrity. Without rapid and efficient resealing, damaged cells would quickly succumb to programmed or necrotic death. Since the 1960s, efforts to understand the plasma membrane resealing process have been motivated by the devastating consequences associated with its dysfunctions. Indeed, diseases such as Limb-Girdle Muscular Dystrophy, diabetes, and Chediak-Higashi Syndrome have been linked to deficient plasma membrane repair due to mutations in the gene encoding dysferlin, production of advanced glycation end products, and defects in the lysosomal trafficking regulator CHS1, respectively[1,2,3,4,5,6]. However, to date, our understanding of membrane resealing is still limited[7]. Initial studies have demonstrated that membrane resealing is initiated by the influx of extracellular Ca^{2+} through the damaged plasma membrane[8,9,10]. Since then, several non-mutually exclusive Ca^{2+}-dependent mechanisms have been proposed to reseal cells. The patch hypothesis proposes that in proximity to the wound, intracellular vesicles fuse with each other and the damaged plasma membrane to act as a patch[11,12,13,14]. A second model proposes that calcium-dependent exocytosis of lysosomes at the wound site releases the lysosomal enzyme acid sphingomyelinase, which converts sphingomyelin to ceramide in the outer leaflet of the plasma membrane. This sudden change in lipid composition results in ceramide-driven endocytosis of the damaged region[15,16,17]. Lastly, the third proposed mechanism involves a role for the endosomal sorting complex required for transport (ESCRT) to promote the formation of outward-facing vesicles that bud off from the plasma membrane[18]. Only a limited set of proteins was identified in these models, and their machinery must be further elucidated.

Here we describe a high-throughput assay that measures the plasma membrane resealing efficiency in adherent mammalian cells subjected to damage mediated by recombinant listeriolysin O (LLO)[19]. LLO is a pore-forming toxin (PFT) secreted by the facultative intracellular pathogen Listeria monocytogenes[20,21,22] and belongs to the MACPF/CDC (membrane attack complex, perforin, and cholesterol-dependent cytolysin) superfamily. MACPF are mammalian pore-forming proteins involved in immune defenses, whereas CDCs are bacterial toxins mainly produced by Gram-positive pathogens that damage host cells to promote their pathogenic lifestyles[23]. CDCs are synthesized as water-soluble monomers

or dimers that bind to cholesterol present in the plasma membrane and oligomerize into a prepore complex of up to 50 subunits. The prepore complex then rearranges to insert β-strands across the lipid bilayer, forming a β-barrel pore that spans 30-50 nm in diameter[24,25,26,27]. These large pores permit fluxes of ions and small cellular components in and out of the cell; though, some studies have proposed that pores of smaller sizes are also formed[28,29,30]. Among the CDCs, LLO displays unique properties including irreversible pH- and temperature-dependent aggregation, which is conducive to high-throughput analyses[31,32]. LLO can be added to the cell culture medium at 4 ˚C, a temperature permissive to its binding to cells, but not to the formation of the pore complex. Initiation of pore formation can then be synchronized by raising the temperature to 37 ˚C, allowing for the efficient diffusion of toxin molecules in the plane of the membrane to form oligomers and for the conformational remodeling involved in pore generation. Therefore, following the switch in temperature, the kinetic of cell damage will depend on the amount of toxin bound to the plasma membrane. Importantly, soluble LLO (not bound to the plasma membrane) rapidly and irreversibly aggregates when the temperature reaches 37 ˚C, which alleviates the need to wash away unbound toxin molecules and limits the extent of membrane damage over time. Lastly, because LLO binds to cholesterol and forms pores in cholesterol-rich membranes, this assay is amenable to a wide range of mammalian cells. It is important to keep in mind that LLO affects host cell signaling mainly via pore formation, with a few exceptions in which pore-independent cell signaling may occur[33,34,35,36,37,38,39]. Therefore, it cannot be excluded that LLO signaling activities may influence the process of membrane repair.

This assay directly assesses the extent of cell wounding by measuring the incorporation of a cell impermeant fluorochrome (*e.g.*, propidium iodide) that passively enters wounded cells and becomes highly fluorescent once it associates with nucleic acids. Hence, the fluorochrome can be maintained in the cell culture medium throughout the experiment, allowing real-time analyses of cell wounding. The fluorescence intensity of the nucleic acid-binding dye will increase with the concentration of toxin and, for a given concentration of toxin, will increase over time until all pores are formed, and cells are fully repaired or until saturation is reached. The influx of extracellular Ca^{2+} through membrane pores is a *sine qua non* event for resealing. Therefore, the resealing efficiency can be indirectly evidenced by comparing cell wounding in culture medium containing Ca^{2+} (repair permissive condition) to wounding in a Ca^{2+}-free medium (repair restrictive condition). Because the fluorescence intensity of the nucleic acid-binding dye is directly proportional to the cell concentration in each well, it is important to seed cells at the same concentration in all wells. It is also important to enumerate cells in each well before and after the assay to ensure that cell detachment does not occur, as floating, aggregated cells can obscure fluorescence readings which may complicate data interpretation. To enumerate cells, cells expressing nuclear-localized histone 2B-GFP (H2B-GFP) were used in this assay. Temperature-controlled, multi-mode, microplate readers combine rapid, high-throughput measurements (using a 96 or 384-well plate format) of fluorescence intensities with microscopy imaging of living cells at 37 °C. The latter can be used to enumerate cell number and observe the eventual formation of distinct cell populations.

Ultimately, this assay provides users the ability to expand their knowledge of the complexity of membrane repair mechanisms by screening for host molecules or exogenously added compounds that may control membrane repair. The following protocol describes the experimental steps to measure the resealing efficiency of cells exposed to LLO and evaluate the effects of a given drug or cellular treatment on resealing efficiency.

Protocol

1. Preparation

1. Cell Plating
   Note: Human cervical epithelial cells, HeLa and HeLa expressing Histone 2B-GFP (H2B-GFP), were used in this protocol, but this assay can be adapted to other mammalian cells[19].
   1. Detach adherent cells from a 75 cm^2 cell culture flask by washing the cells with 2 mL of Trypsin-EDTA 0.25%. Replace the used trypsin with 2 mL of fresh trypsin-EDTA 0.25%.
   2. Incubate the cells at 37 ˚C for 5 min until the cells have rounded and detached from the flask.
   3. Resuspend the cells in 8 mL of growth medium (DMEM containing 10% heat-inactivated fetal bovine serum, 100 U/mL penicillin, and 100 µg/mL streptomycin).
   4. Determine the cell concentration using a hemocytometer and 10 µL of cell suspension.
   5. Dilute the cells in growth medium to a concentration of 2.5 x 10^5 cells/mL.
   6. Pour the cell suspension into a sterile pipette basin and thoroughly mix the suspension using a 10 mL serological pipette.
   7. Using a 12-multichannel micropipette and 200 µL tips, distribute HeLa cells (2.5 x 10^4 cells/100 µL/well) in triplicate (or quadruplicate) in a 96-well flat, clear bottom, black polystyrene tissue culture-treated plate.
      Note: A plating arrangement is presented as an example in **Figure 1**.
   8. Culture the cells for 24 h in a humidified cell culture incubator at 37 ˚C and 5% CO_2.

2. **Stock Solution Preparation**
   1. Prepare 1 L of a 10x stock of buffer M (used to prepare M1 and M2) by adding 95 g of Hanks Balanced Salt Solution, 0.476 g of $MgCl_2$ (5 mM), and 23.83 g of HEPES (100 mM) to 900 mL of water. Adjust the pH to 7.4 and raise the volume to 1 L. Filter sterilize.
   2. Prepare 50 mL of a 50x (1.25 M) stock of glucose by adding 11.26 g of D-(+)-Glucose to a total of 50 mL of water. Filter sterilize the solution.
   3. Prepare 50 mL of a 100x (120 mM) stock of calcium by adding 0.666 g of $CaCl_2$ to a total of 50 mL of water. Filter sterilize the solution.
   4. Prepare 50 mL of a 10x (50 mM) stock of ethylene glycol-bis(2-aminoethylether)-N,N,N',N',tetraacetic acid (EGTA) by adding 0.951 g of EGTA to 40 mL of water. Increase the pH to 8 using NaOH to dissolve the EGTA, then raise the volume to 50 mL. Filter sterilize the solution.
   5. For a single 96-well plate, prepare 50 mL of Medium 1 (M1, contains Ca^{2+}), 50 mL of Medium 2 (M2, Ca^{2+}-free), and 15 mL of Medium 2 supplemented with EGTA, accordingly:
      1. For M1, add 5 mL of 10x Buffer M, 0.5 mL of 100x $CaCl_2$, and 1 mL of 50x glucose to 43.5 mL of water.
      2. For M2, add 5 mL of 10x Buffer M and 1 mL of 50x glucose to 44 mL of water.
      3. For M2/EGTA, add 1.5 mL of 10x Buffer M and 1.5 mL of 10x EGTA to 12 mL of water.

Note: All solutions containing propidium iodide (PI) should be prepared directly prior to adding to the cells.

3. Plate Reader/Imaging Cytometer Settings
   Note: Use a multi-mode plate reader equipped with two detection units: a spectrofluorometer and an imaging cytometer. Limit the fluorescence exposure to avoid photobleaching the fluorophores.
   1. Pre-warm the plate reader to 37 °C before performing the assay.
   2. Set up the parameters for the kinetic assay accordingly within the **Settings** mode:
      1. Choose **Monochromator**, **FL (fluorescence)**, and **Kinetic** for the optical configuration, read modes, and read type, respectively.
      2. Under **Wavelength Settings**, select a 9 and 15 nm excitation and emission bandpass, respectively. For assays using propidium iodide (PI), set the excitation and emission wavelengths to 535 and 617 nm, respectively.
      3. Under **Plate Type**, select **96 Wells** for the plate format and a pre-set plate configuration corresponding to a black-wall clear bottom plate.
      4. Under **Read Area**, highlight the wells that will be analyzed throughout the kinetic.
      5. Under **PMT and Optics**, preset the flashes per read to **6** and check the box for **Read from Bottom**.
      6. Under **Timing**, insert **00:30:00** in the **Total Run Time** box for a 30 min kinetic assay, and insert **00:05:00** for the **Interval**.
         Note: For each time point and one wavelength, the reading time of a full 96-well plate is 30 s.
      7. Confirm the specified settings in the **Settings Information** to the right and select **OK**. Press **Read** to initiate the kinetic run.

   3. Set up the imaging parameters accordingly within the Settings mode:
      1. Choose **Minimax**, **Imaging**, and **Endpoint** for the optical configuration, read modes, and read type, respectively.
      2. Under **Wavelengths**, select **transmitted light**, and either or both the fluorescence boxes corresponding to excitation and emission wavelengths of 456/541 nm (GFP) and 625/713 nm (PI).
      3. Use the same options for the **Plate Type** and **Read Area** as defined in steps 1.3.2.3 and 1.3.2.4.
      4. Under **Well Area Setting**, select the number of sites within a well to be imaged.
         Note: 12 sites correspond to a full-well image.
      5. Under the **Image Acquisition Settings**, select the exposure times for transmitted light, 541 (GFP), and 713 (PI). For GFP, image the entire well with an exposure time of 20 ms/image. For transmitted light (TL) and PI fluorescence, acquire a single image of the center of each well with exposure times of 8 and 20 ms, respectively.
      6. Confirm the specified settings in the **Settings** Information to the right and select **OK**. The acquisition time for imaging the entire surface of each well (12 images/well) of a 96-well plate and for one wavelength is ~15 min. Press **Read** to initiate imaging.
         Note: The acquisition time of a single image/well of a 96-well plate requires ~2.5 min/plate for one wavelength. The parameters described above correspond to the specific equipment in our laboratory. Spectrofluorometric measurements: A xenon flash lamp displaying 1.0 nm increment excitation wavelengths (250-850 nm) with an adjustable 9 or 15 nm bandpass, a photomultiplier tube detector with a > 6 log dynamic range and an adjustable 15 or 25 nm emission bandpass. Imaging cytometer: An illumination light source capable of white light, 460 nm and 625 nm excitation wavelengths with a 20 nm bandpass, emission filters centered at 541 nm (108 nm bandpass) and 713 nm (123 nm bandpass), respectively, and a 4X objective coupled to a 1.25 megapixel 12-bit charge-coupled device camera.

2. Assay

Note: At the time of the assay, cells must be 70-90% confluent. During the wash steps, the medium should be removed from and applied to the side-wall of the well (not directly above the cells). Maintain the temperature of LLO at < 4 ˚C to prevent its aggregation until step 3.1.5.

1. Prepare a stock of 30 µM PI in M1 and a stock of 30 µM PI in M2 pre-warmed at 37 ˚C.
2. Gently wash the cells in plate 1 using a 12-multichannel micropipette and 200 µL tips, as follows:
   1. For repair-permissive conditions, remove the growth medium and wash the cells twice with 200 µL/well M1 pre-warmed at 37 ˚C. Replace the medium with 100 µL/well of warm M1 containing 30 µM PI.
   2. For repair restrictive-conditions, remove the growth medium and wash the cells once with 200 µL/well warm M2 containing 5 mM EGTA to chelate Ca^{2+}, followed by one wash with 200 µL/well M2. Replace the medium with 100 µL/well warm M2 containing 30 µM PI.
   3. After the growth medium has been washed and replaced with medium containing propidium iodide, directly move to step 2.1.3.

3. Image plate 1 under transmitted light, GFP, and PI as detailed under 1.3.3 (pre-kinetic). This step takes 15-20 min.
4. During the 15 min period in step 2.1.3, prepare plate 2 using a 12-multichannel micropipette and 200 µL tips as follows:
   1. Place a 96-well round bottom polypropylene microplate on ice. Configure the plate using an experimental design corresponding to plate 1 (**Figure 1**).
   2. For repair-permissive conditions, add 100 µL/well of ice-cold M1 containing 60 µM PI, followed by the addition of 100 µL/well of ice-cold M1 containing 4x LLO or not for the control.
   3. For repair-restrictive conditions, add 100 µL/well of ice-cold M2 containing 60 µM PI, followed by the addition of 100 µL/well of ice-cold M2 containing 4x LLO or not for the control.

5. After imaging plate 1 (step 2.1.3), immediately place it on ice, using aluminum foil to separate the plate from direct contact with ice. Allow plate 1 to cool down for 5 min.
6. Using a 12-multichannel micropipette and 200 µL tips, transfer 100 µL from each well into plate 2 (step 2.1.4) to the corresponding wells in the plate 1. To properly distribute the toxin in the media of plate 1, insert the tips below the meniscus and gently eject the volume without introducing bubbles.
   Note: Do not pipette up and down, as this may inadvertently detach the cells.

7. Leave the plate for an additional 1 min to allow the toxin to bind to the cells and immediately transfer plate 1 to the plate reader for the kinetic assay using the spectrofluorometer mode (step 1.3.2).
8. At the end of the kinetic assay, immediately image plate 1 (post-kinetic) using step 1.3.3.

3. Analysis: Cell Enumeration

1. Determine the cell count based on the nuclear fluorescence using the microplate cell enumeration software.
    1. Within **Settings,** select **Re-analysis**, and under the category section within the **Image Analysis Settings** select **Discreet Object Analysis** using **541** as the wavelength for finding objects.
    2. Within the Find Objects option, using the **Draw on Images** finding method, select **Nuclei** under the settings tab, and press **Apply**.
    3. Press **OK** and **Read** to initiate the cell counting algorithm.

2. Alternatively, if no such tool is available, use an image analysis software such as ImageJ to enumerate cells.
    1. In ImageJ, open the image file as a stack.
    2. Convert the stack to 8-bit greyscale images by clicking **Image** in the menu bar, hover over **Type,** and select **8-bit**.
    3. Subtract the background: Click **Image** in the menu bar, hover over **Adjust**, and select **Brightness/Contrast**. Adjust the minimum value to remove the background noise and select **Apply**.
    4. Threshold to create binary images: Click **Image** in the menu bar, hover over **Adjust**, and select **Threshold**. Select **Dark background**, adjust the minimum and maximum threshold values, and click **Apply**.
    5. In the case of overlapping nuclei, a Watershed tool can be used to segment nuclei. Click **Process** in the menu, hover over **Binary** and select **Watershed**.
    Note: This will automatically separate connected nuclei.
    6. Analyze the masked images by applying user-specified criteria (size and circularity) to refine the identification of nuclei and exclude cell debris.
        1. Click on **Analyze** in the menu and then **Analyze particles**. Set the desired size (pixel^2) and circularity (a value of 1 is a perfect circle) ranges that are sufficient to include individual cells/nuclei.
        2. In the Show dropdown box, select the option(s) desired, check **Summarize**, and click **OK** to obtain cell counts.

4. Analysis: Kinetic Curves

1. Transfer the kinetic data from the plate reader software to an analytical data software.
2. For each experimental condition, average the fluorescence intensities of the replicates at each timepoint, along with the corresponding standard deviation and standard error of the mean for each experimental condition.
3. For each experimental condition, trace the corresponding kinetic curve: PI intensity (y-axis) versus time (x-axis).
4. To calculate the resealing efficiency of a given treatment condition, calculate the area under the curve (AUC) of the +LLO in M1 (AUC(M1)) and +LLO in M2 (AUC(M2)). Use the approach suggested below to assess the efficiency (E) of resealing:

$$E = 1 - \left[\frac{AUC(M1)}{AUC(M2)}\right] = \frac{AUC(M2) - AUC(M1)}{AUC(M2)}$$

5. Perform a comparison between control and test treatment by determining the efficiency ratio (R_{Eff}) indicated below:

$$R_{EFF} = \frac{Etest}{Econtrol} = \frac{AUC(control,\ M2)}{AUC(test,\ M2)} * \left[\frac{AUC(test,\ M2) - AUC(test,\ M1)}{AUC(control,\ M2) - AUC(control,\ M1)}\right]$$

R_{EFF} = 1, test treatment has no effect on repair
R_{EFF} < 1, test treatment inhibits repair
R_{EFF} > 1, test treatment improves repair

6. Calculate the area under the curve using the following equation:

$AUC = \sum_{i=1}^{k-1}(Intensity_{i+1} + Intensity_i) \times (Time_{i+1} - Time_i)/2$, where k is the total number of follow-ups.

Representative Results

Cell counting accuracy: HeLa cells are frequently used as a model mammalian cell line to explore membrane repair mechanisms. When assessing membrane repair at the cell population level, it is important to plate cells at the same concentration in all wells for proper data interpretation. It is also important to verify at the time of the assay that cell numbers are equivalent across wells. HeLa cells that constitutively express histone 2B fused to GFP (H2B-GFP) were introduced in this assay to automatically enumerate cells based upon detection of their fluorescent nuclei. To establish the accuracy in cell enumeration, twofold serial dilutions of HeLa H2B-GFP cells were plated in triplicate in a 96-well plate and cultured for 4 h. This amount of time is sufficient for cell attachment and provides limited cell division. Full wells were imaged under transmitted light (TL) and GFP fluorescence illuminations and cell counts were assessed based on GFP fluorescence using the plate reader analysis software (**Figure 2A** and **2B**). The average cell counts ± standard deviation was plotted against cell seeding concentrations, and a line of best fit indicated a 1.08:1 ratio of cell count to cell seeding, demonstrating the accuracy of the counting (**Figure 2C**). By imaging all of the wells prior to a kinetic assay, it can be ensured that cell numbers are consistent among all wells. Also, by imaging wells after the kinetic assay, one can establish if exposure to the toxin caused cell detachment.

Expression of GFP does not interfere with propidium iodide (PI) intensity measurements (I_{PI}): to ensure that H2B-GFP nuclear association does not interfere with PI incorporation or PI fluorescence intensity measurement (I_{PI}), I_{PI} was compared in HeLa and HeLa H2B-GFP cells that were exposed, or not, to 1 nM LLO (**Figure 3**). In the absence of PI, there was a similarly low level of background fluorescence in HeLa and HeLa H2B-GFP, indicating that GFP does not bleed through PI fluorescence emission filters. In the presence of PI, but absence of LLO, there was a similar basal PI fluorescence emission in both HeLa and HeLa H2B-GFP that did not change over time. This confirmed that expression of GFP does not affect measurement of PI fluorescence and indicated that PI does not penetrate non-damaged cells over the time frame of the experiment. Addition of LLO resulted in an increase in PI fluorescence over time that was similar in both HeLa and HeLa H2B-GFP. This increase is due to cell wounding by LLO combined with PI association with nucleic acids. Together, these results establish that expression of histone-2B-GFP does not affect PI incorporation or measurement of its fluorescence.

PI fluorescence does not interfere with GFP-based cell counting: Reciprocally, it was important to verify that PI nuclear incorporation in wounded cells does not interfere with GFP-based cell counting. Representative fluorescence images of HeLa and HeLa H2B-GFP exposed to 1 nM LLO in the presence of PI showed that there was a marked accumulation of PI in wounded cells post kinetics, as expected (**Figure 4A**). Imaging also revealed that PI could bleed through GFP fluorescence detection (**Figure 4A** and **Table 1**). This fluorescence crossover was best appreciated on the post-kinetic images of HeLa cells that do not express GFP, but still displayed green fluorescent nuclei (**Figure 4A**). This crossover could also be evidenced by the measurement of GFP fluorescence intensity (I_{GFP}) in HeLa H2B-GFP cells, which significantly increased post-kinetic compared to pre-kinetic (**Figure 4B**). Importantly, PI fluorescence crossover does not affect cell counting because the segmentation process involved in the enumeration of nuclei is unaffected by an increase in GFP fluorescence (**Figure 4C**).

Measuring plasma membrane resealing efficiency: In this section, we present the basic methodology used to measure the efficiency of membrane resealing. To evidence the process of membrane resealing, HeLa H2B-GFP cells were exposed, or not, to 1 nM LLO in the presence (M1) or absence (M2) of extracellular Ca^{2+} (**Figure 5**). As expected, in the absence of LLO, I_{PI} remained constant in M1 and M2. Addition of LLO in Ca^{2+}-containing medium resulted in a steady increase in PI fluorescence intensity (I_{PI}), whereas in the absence of extracellular Ca^{2+}, there was a significantly steeper increase in PI fluorescence, reflecting the absence of membrane resealing. To assess the resealing efficiency, which is defined as the capacity of cells to repair in M1 relative to M2 (step 1.5.4.1), the area under the M1 and M2 curves (AUC) were determined and the efficiency of repair (E) was calculated to be 0.287.

An alternative to PI: PI has been ubiquitously used as a marker for plasma membrane damage. However, there are other nucleic acid binding dyes that are also suitable for this assay. For example, a membrane impermeant carbocyanine nucleic acid binding dye (CNABD) exhibits an emission spectrum reaching into the far red and has a high specificity for double stranded DNA. PI on the other hand binds both DNA and RNA[40,41]. Unlike PI, the excitation and emission spectra of CNABD does not overlap with those of GFP allowing for better spectral resolution between the two fluorochromes. Furthermore, the CNABD used in this protocol has an extinction coefficient nearly twice that of PI, which means that for their respective excitation wavelengths, this dye is more capable of absorbing energy than PI resulting in a stronger fluorescence emission. Quantitative fluorescence analysis of CNABD and GFP images showed that this dye exhibits a large fluorescence dynamic range, does not significantly emit at the wavelengths of GFP fluorescence, and does not affect cell count (**Figure 6A-D**). Indeed, HeLa H2B-GFP cells incubated in M1 or M2 media containing CNABD and damaged by 1 nM LLO exhibited a 4- and 5.5-fold increase in I_{CNABD} relative to the non-damaged controls, respectively (**Figure 7A**). For comparison, cells exposed to 1 nM LLO in the presence of PI exhibited a 2.5- and 3-fold increase in PI fluorescence intensity in M1 and M2, respectively (**Figure 5**). Like PI, CNABD exhibits increasing fluorescence intensity with increasing LLO concentration in M1 (**Figure 7A**), and the resulting repair efficiency was calculated as described in step 1.5.4.1 (**Figure 7B**). We report that the cell resealing efficiency decreases as LLO concentration increases. This phenomenon reflects the fact that cells decrease their capacity to reseal when excessive damages are caused.

Quality assessment of the membrane repair assay: a critical aspect of any assay is its robustness or capability to detect and resolve differences between the negative and positive controls. Signal variation between positive and negative controls must display sufficient dynamic range and reproducibility. In this membrane repair assay, the positive and negative controls are cells exposed to LLO in repair-permissive (M1) and repair-restrictive (M2) conditions, respectively. Two approaches were taken to assess the robustness of this assay for high-throughput analysis. First, the Z-factor, or screening window coefficient, determines whether a given set of conditions provides a large enough dynamic range, while accounting for signal variability. Z-factors within the ranges $0 < Z \leq 0.5$ and $0.5 < Z \leq 1$ correspond to an acceptable and very good assay, respectively[42,43]. A limitation of using the Z-factor for quality assessment is that tested conditions typically exhibit more moderate values compared to the extreme positive and negative controls. Therefore, as a second approach, we calculated the strictly standardized mean difference (SSMD, β), which can identify differences between experimental conditions that would otherwise be categorized as a negative result based on a qualified Z-factor[44,45]. SSMD values can be categorized into effect strength ranging from no effect ($\beta = 0$) to extremely strong ($\beta \geq 5$). Using the data from **Figure 7A** and AUC for comparison of M1 versus M2 conditions, exposure to 0.25 and 0.5 nM LLO produced Z-factor values of 0.3100813 and 0.137313, and $\beta = 6.0672$ and 4.803308, respectively, indicating that a window of LLO concentrations is suitable for the assay. As the concentration of LLO is increased beyond 1 nM, the gap in the I_{CNABD} kinetic curves between M1 and M2 conditions closes resulting in drastically reduced Z-factor and SSMD values (**Figure 7B**). Such high concentrations of LLO correspond to conditions in which the repair potential is outweighed by damage and thus negates the use of the assay in identifying factors involved in membrane repair. This is further illustrated by the decrease in repair efficiency (E) as LLO concentration increases (**Figure 7B**). All data (Z-factor, SSMD, and E) were generated with 3 biological replicates and 3 technical replicates per experimental condition for assay validation. Together, these data show that this assay has the expected robustness for a high-throughput assay with LLO concentrations inferior to 1 nM for HeLa cells.

Proof of principle: Once the robustness of the assay was established, we performed additional experiments as a proof of principle that this assay has the sensitivity and resolution to identify a defect in the repair process. Also, we considered that high-throughput assays are used as a screening process to identify "hits" within large screens, which may involve less than 3 biological replicates. Thus, it is pertinent that the experimental design provides the detection power to identify "hits" within a single assay. Therefore, under a high-throughput screen, the assay layout can be adjusted to accommodate 4 technical replicates to increase statistical power in a single experiment. Cells were plated in quadruplicate and were pre-treated 1 h prior to the assay with desipramine, a pharmacological inhibitor of the lysosomal protein acid sphingomyelinase (ASM) which plays a role in plasma membrane repair[15,17,46]. Importantly, treatment with desipramine did not affect cell counts throughout the assay, allowing for appropriate comparison between desipramine-treated and non-treated cells (**Figure 8A**). Inhibition of ASM in desipramine-treated cells resulted in a defect in membrane resealing efficiency upon exposure to LLO, as illustrated by the decrease in E and R_{Eff} (**Figure 8B** and **8C**). Using a mixed effects model, a comparison of desipramine-treated to non-treated cells exposed to 0.25 and 0.5 nM LLO in M1 showed p-values of 0.0010 and 1×10^{-10}, respectively. Together, data indicate that 0.25 and 0.5 nM LLO are appropriate concentrations to identify defects in repair in a high-throughput experimental setting, with possible statistical analyses of a single experiment once the technical replicates are increased to four. Note that the statistical approach of the mixed effects model between quadruplicate will not account for potential variations across multiple biological replicates. Any significant findings using one biological replicate should be verified in additional experimental settings.

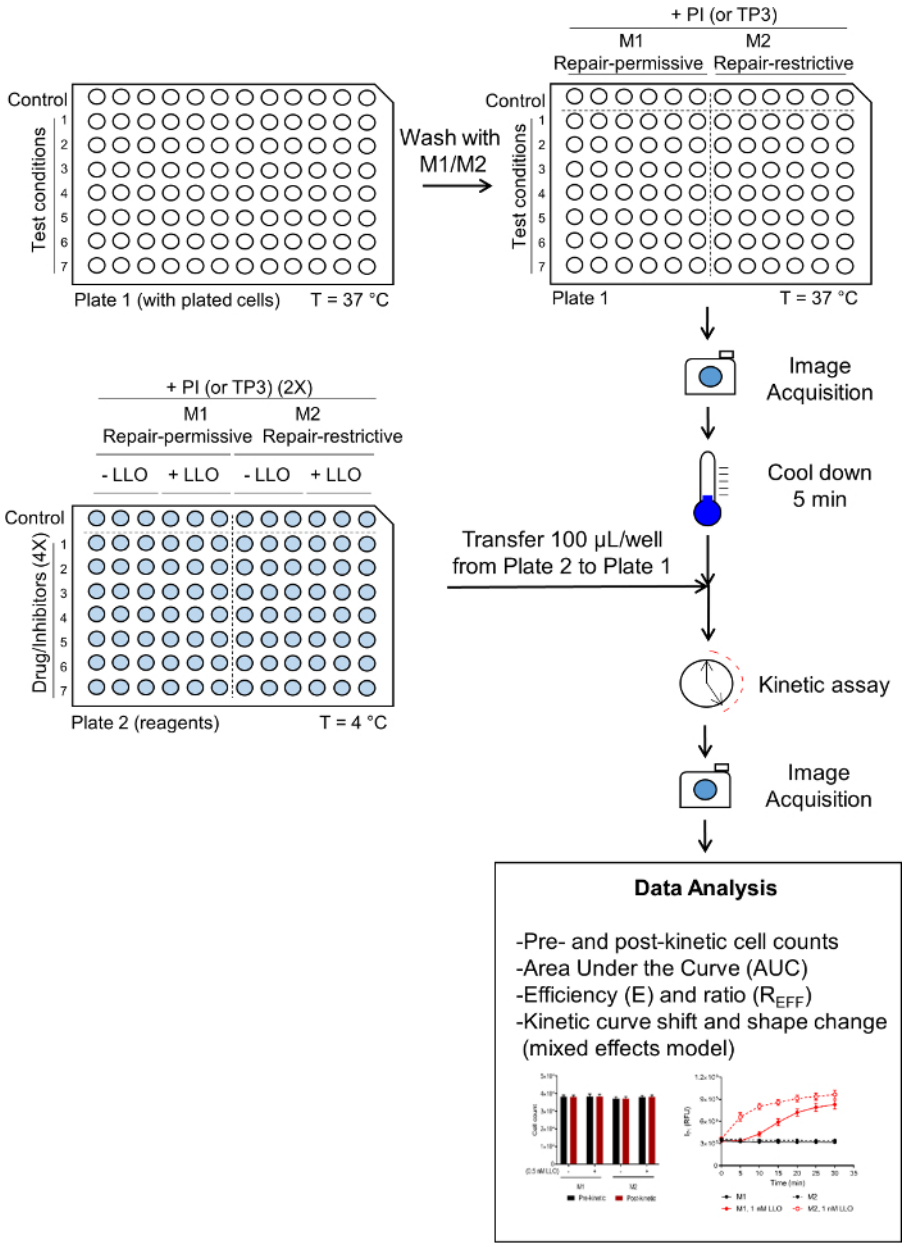

Figure 1: Experimental design. The flow diagram depicts a representative plate design configured to test the effect of seven test conditions in comparison to control non-treated cells. Additional controls should be included if appropriate, as for example drug vehicles. Cells are plated (plate 1) 24 h prior to the experiment. On the day of the experiment, cells in plate 1 are washed with M1 or M2 medium pre-warmed at 37 °C, and the plate is imaged (TL, GFP and PI fluorescence) pre-kinetic. During the 15 min of imaging, reagents are added on ice to plate 2. After imaging, plate 1 is immediately placed on ice for 5 min, and 100 µL/well are transferred from plate 2 to plate 1. Plate 1 is placed in the plate reader to run the kinetic assay at 37 °C for 30 min, followed by imaging (TL, GFP, and PI fluorescence). Data are then analyzed to count cells and assess repair efficiency in all experimental conditions. In large data sets, analysis can be automated. Also, the number of technical replicates can be increased to 4 in high-throughput screens. Please click here to view a larger version of this figure.

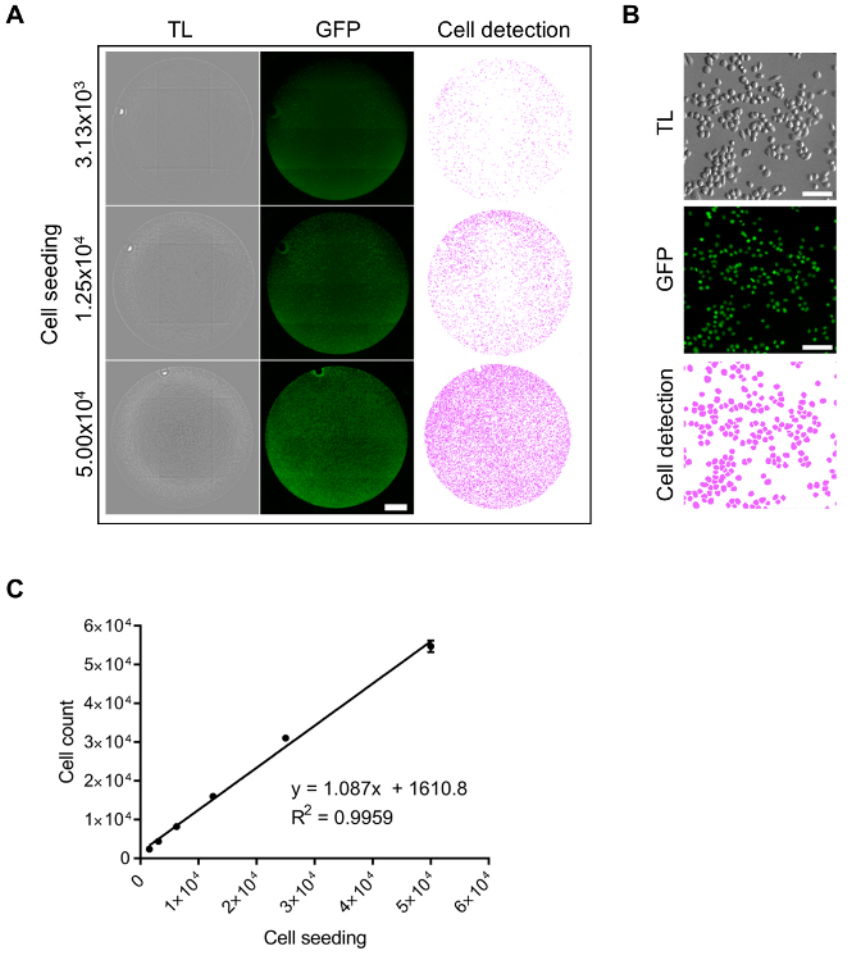

Figure 2: Cell counting accuracy. HeLa cells expressing GFP-tagged Histone 2B were seeded in triplicates at the indicated concentrations. (**A**) Cells were imaged at 37 °C under transmitted light (TL) and GFP fluorescence (12 images/well) and a cell detection algorithm was used to delineate individual nuclei (in purple). Scale bar = 1 mm. (**B**) Higher magnification of TL, GFP, and cell detection (purple) images (zoomed 2X). Scale bar = 100 µm. (**C**) Image analysis software was used to count the number of cells and the cell counts were plotted against the initial cell seeding concentration. Please click here to view a larger version of this figure.

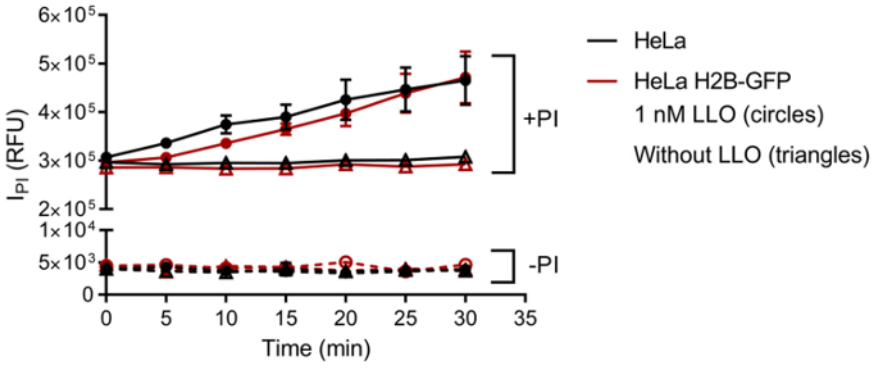

Figure 3: Propidium iodide fluorescence measurement is not affected by Histone 2B-GFP expression. Histone 2B-GFP expressing and non-expressing HeLa cells were exposed, or not, to 1 nM LLO in the presence (solid lines) or absence (dashed lines) of 30 µM PI in Ca^{2+}-containing medium (M1). The kinetic assay measured PI fluorescence intensities by spectrofluorometry every 5 min for 30 min at 37 °C. Data are the average PI fluorescence intensity (I_{PI}) expressed in relative fluorescence units (RFU) ± SEM (n = 3 independent experiments, each performed in triplicates). Please click here to view a larger version of this figure.

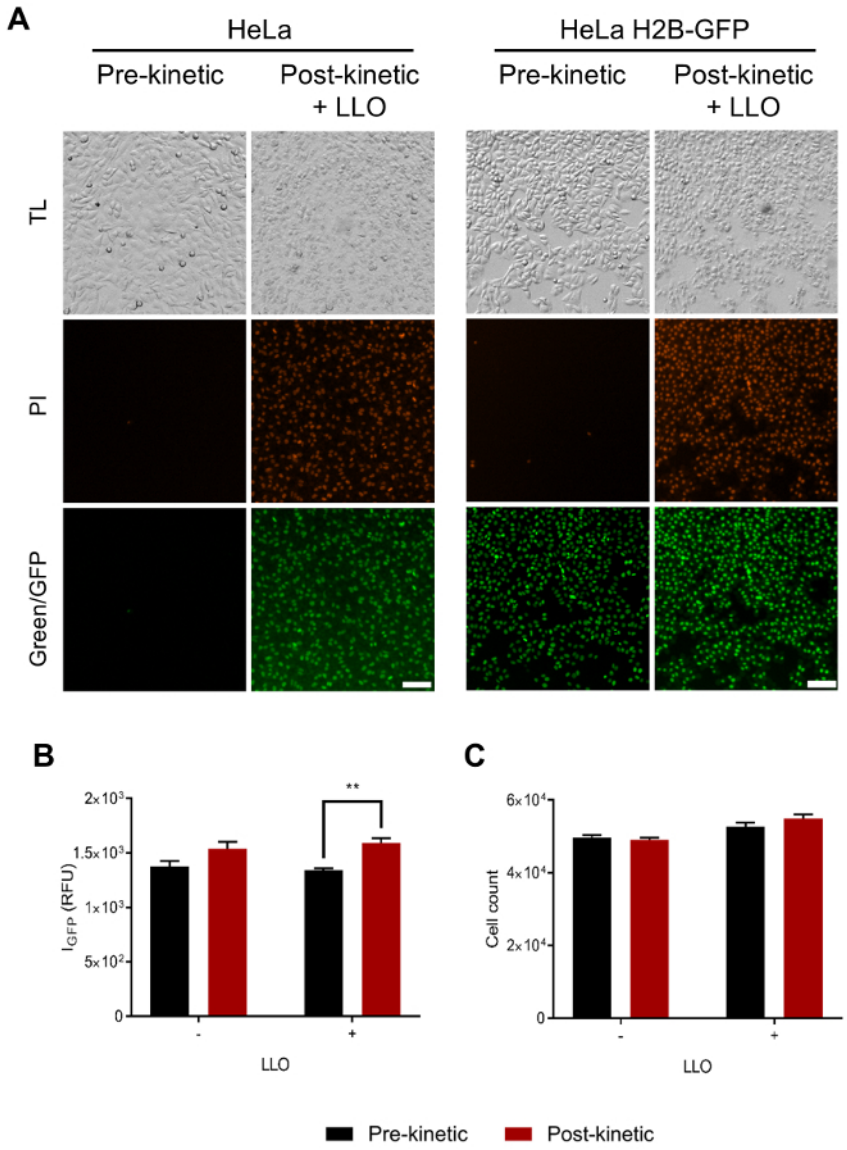

Figure 4: Cell enumeration is unaffected by PI fluorescence. (**A**) Representative pre- and post-kinetic images (TL, PI, and GFP) of cells exposed, or not, to 1 nM LLO in M1. Scale bar = 100 µm. (B) Quantitative fluorescence microscopy analysis (I_{GFP}± SEM) revealed the increased GFP fluorescence measurement due to PI nuclear incorporation upon cell wounding by LLO (post-kinetic). (**C**) GFP-based cell enumeration was unaffected by the increase in GFP intensity. Cell count per well was expressed as average ± SEM. (In B and C: black bars = pre-kinetic data; red bars = post-kinetic data; n = 3 independent experiments, each performed in triplicates; a two-tailed Student's t-test was used to analyze quantitative fluorescence intensity and cell counts from acquired images, **p < 0.01). Please click here to view a larger version of this figure.

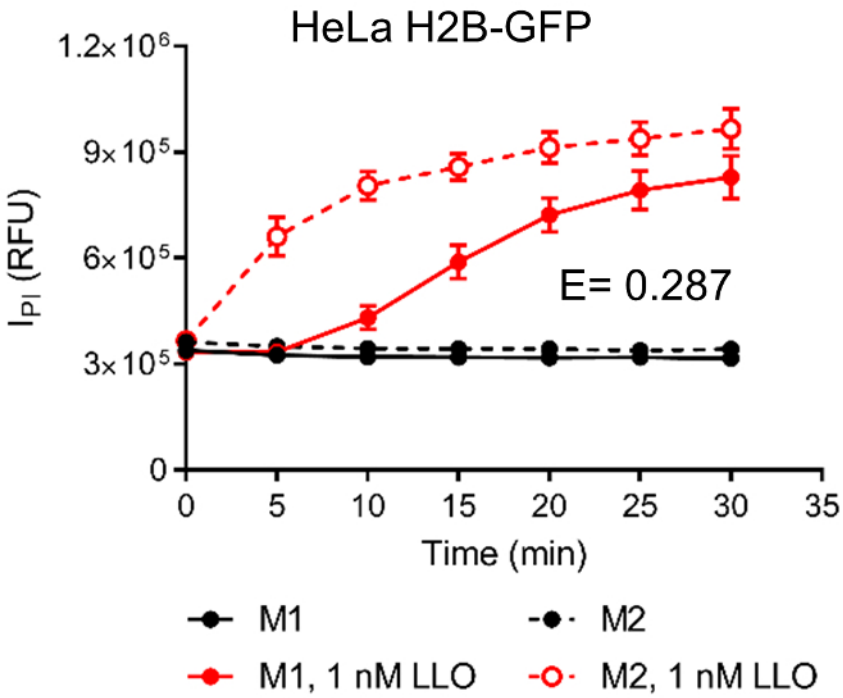

Figure 5: Measuring plasma membrane resealing efficiency. Histone 2B-GFP expressing HeLa cells were exposed, or not, to 1 nM LLO in Ca^{2+}-containing (M1) or Ca^{2+}-free (M2) medium containing 30 µM PI. Kinetic data represent PI fluorescence intensity (I_{PI}) in relative fluorescence units (RFU) ± SEM, measured for 30 min at 37 °C. n = 3 independent experiments, each performed in triplicates. The resealing efficiency was measured as indicated in protocol step 1.5.4. Please click here to view a larger version of this figure.

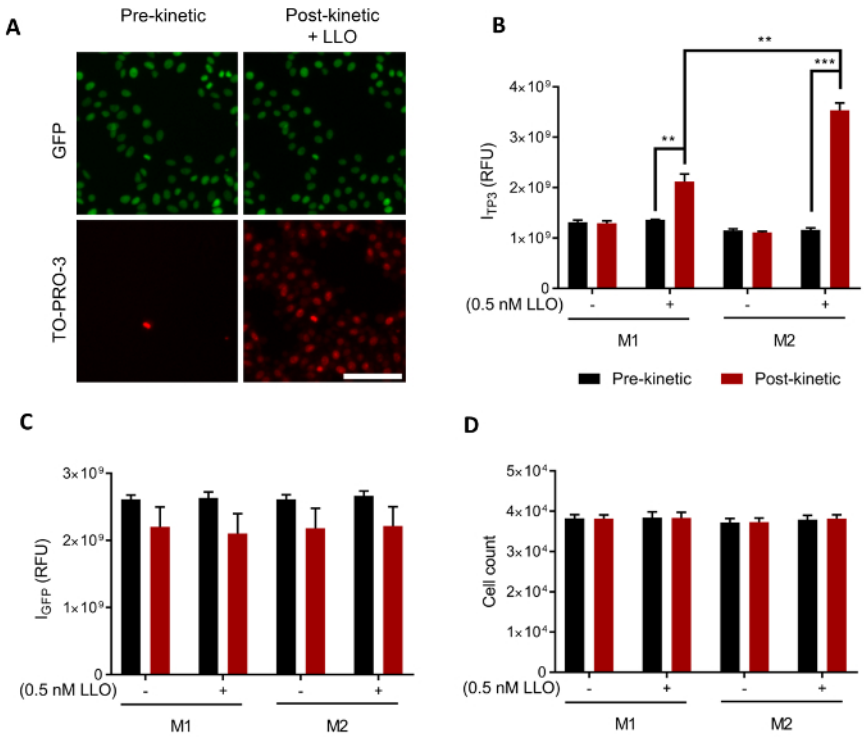

Figure 6: Carbocyanine nucleic acid binding dye as an alternative dye to assess membrane resealing. HeLa H2B-GFP cells were exposed, or not, to 0.5 nM LLO for 30 min at 37 °C in the presence of 1 µM CNABD in Ca^{2+}-containing (M1) or Ca^{2+}-free (M2) medium. (**A**) Images of HeLa H2B-GFP cells were acquired pre- and post-kinetic in M1 containing the dye. Scale bar = 100 µm. (**B** and **C**) Integrated CNABD and GFP fluorescence intensities were measured using the imaging cytometer and expressed in relative fluorescence units (RFU) ± SEM. (**D**) GFP fluorescence images were processed to enumerate HeLa H2B-GFP cells (black bars = pre-kinetic data, red bars = post-kinetic data, n = 3 independent experiments, each performed in triplicates). A two-tailed Student's t-test was used to analyze quantitative fluorescence intensity and cell counts from acquired images, **p < 0.01, ***p < 0.001) Please click here to view a larger version of this figure.

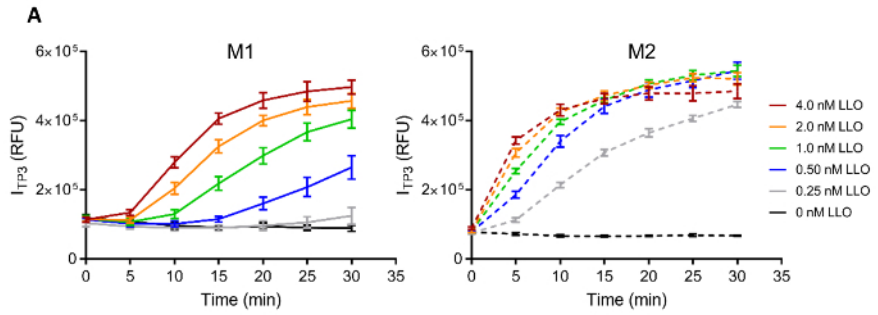

B

LLO (nM)	AUC(M1)	AUC(M2)	Z-factor	SSMD (β)	E
0.25	2966852	8323250	0.372	6.715	**0.643546**
0.50	4395097	1140392	0.064	4.494	**0.614647**
1.00	6912908	12293067	-0.491	2.780	**0.437658**
2.00	8837675	12647264	-1.953	1.431	**0.301218**
4.00	10329587	12400673	-21.721	0.186	**0.167014**

Figure 7: Effect of LLO concentration on resealing efficiency, Z-factor, and SSMD. (**A**) HeLa H2B-GFP cells incubated in M1 or M2 containing 1 µM CNABD were exposed to increasing concentrations of LLO and subjected to the kinetic assay for 30 min at 37 °C. Data are expressed as CNABD intensity (I_{CNABD}) in relative fluorescence units (RFU) ± SEM. (**B**) The Z-factor and strictly standardized mean difference (SSMD) were calculated as a quality assessment for the robustness of the membrane repair assay, using the area under the curve (AUC) as a metric for the kinetic curves[42,43,44,45]. The resealing efficiencies were calculated as described in the protocol and results sections (n = 3 independent experiments, each performed in triplicates). Please click here to view a larger version of this figure.

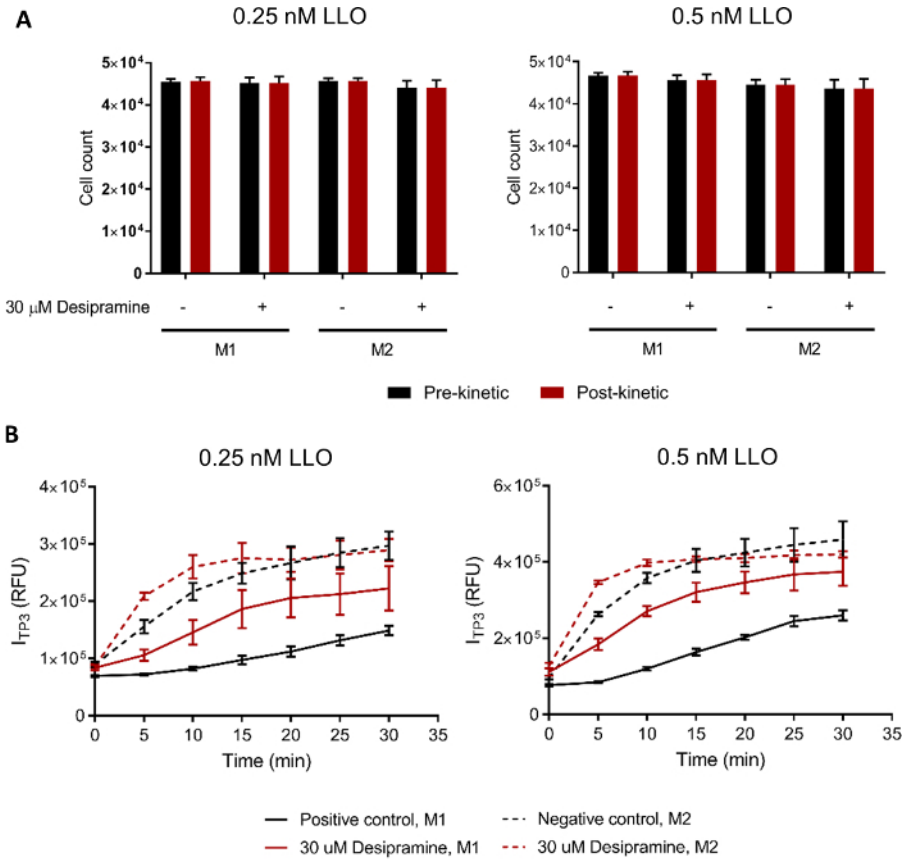

C

	0.25 nM LLO	0.5 nM LLO
$E_{Control}$	0.5575	0.5266
$E_{Desipramine}$	0.3206	0.2433
R_{Eff}	**0.5752**	**0.4621**
***p-value* (mixed effect model)**	**0.0010**	**$1x10^{-10}$**

Figure 8: Cell exposure to desipramine causes defects in resealing. HeLa H2B-GFP cells (plated in quadruplicate) were pre-treated with 30 μM desipramine (or not) for 1 h at 37 °C and then exposed to 0.25 or 0.5 nM LLO in the presence of 1 μM CNABD in Ca^{2+}-containing (M1) or Ca^{2+}-free (M2) medium. Cells were imaged (pre- and post-kinetic) and subjected to the kinetic assay at 37 °C for 30 min. (**A**) Cells were enumerated; data are expressed as average cell counts ± SEM. (**B**) CNABD fluorescence intensity (I_{CNABD}) is expressed in relative fluorescence units (RFU) ± SEM. (**C**) Resealing efficiencies were calculated in the presence and absence of desipramine. A mixed effects model was used on log-transformed intensity values assuming a random intercept for each technical replicate. To capture both a shift and change in shape of the kinetic curves, the main effect of treatment condition and the interaction effect between treatment condition and time were jointly tested for statistical significance. A two-tailed Student's t-test was used to analyze cell counts from acquired images. The p-value was calculated using the mixed effects model. (4 technical replicates, one experiment). Please click here to view a larger version of this figure.

		Imaging Cytometer Emission Channel Specifications	
Fluorophore	Fluorophore ex/em (nm)	Green channel (ex/em ± bandpass, nm)	Red channel (ex/em ± bandpass, nm)
GFP	488/510	460/541 ± 20/108	625/713 ± 20/123
PI	533/617		
CNABD	642/661		

Table 1: GFP, PI, and CNABD excitation and emission peaks and the green and red channel excitation and emission bandpasses for the imaging cytometer.

Discussion

This assay measures the efficiency of membrane resealing at the cell population level with high-throughput capacity. It can be used to screen for cellular components or drug libraries that could affect membrane repair. The described assay used a 96-well plate format, but it can be adapted

to 384-well plates for higher throughput. An advantage of this assay is its ability to obtain fluorescence measurements of adherent living cells in real time without the need for excessive cell processing such as cell detachment, fixation, or fluorescence labeling post-fixation. Multimode plate readers, such as the one used in this protocol, have sufficient sensitivity for rapid spectrofluorometric measurements at time intervals as low as 30 s for a 96-well plate. The acquisition of fluorescence images provides additional information including cell enumeration, eventual changes in cell morphology, and potential identification of distinct cell populations. The present assay does not establish the kinetics of plasma membrane resealing at the single cell level, but identifies experimental conditions (pharmacological compounds or cellular components) that can affect, positively or negatively, the process of membrane resealing at the cell population level.

Several other experimental approaches have been developed to assess the membrane resealing mechanisms. For example, mechanical disruption by microneedle puncture, bead abrasion, and laser ablation have been used to model mechanical membrane damage. The measurement of wounding/repair has involved fluorescence microscopy or flow cytometry by quantifying the entry of fluorescent probes (FM 1-43, propidium iodide, fluorescein-conjugated dextrans) or tracking fluorescent protein chimeras[47,48,49,50]. Each of these approaches has its own advantages; however, they are not amenable to high-throughput screening in living cells as presented in this assay.

The present assay was optimized to analyze the resealing efficiency of cells wounded by the pore-forming protein LLO, which forms large pores that permit the massive Ca^{2+} influx as provoked by mechanical ruptures of the plasma membrane. Although pore-forming toxins represent one form of plasma membrane damage, repair of large toxin pores and mechanical wounds were proposed to share common Ca^{2+}-dependent pathways[17,51]. It is important to note that LLO interaction with cell membrane components such as cholesterol may affect cell signaling and thereby may influence membrane resealing mechanisms when compared to mechanical wounds. Our knowledge about membrane repair is still limited and further studies are required to establish if resealing of mechanical wounds differ from resealing following the formation of toxin pores. There are several advantages of using LLO. First, the initiation of membrane damage can be synchronized by raising the temperature from 4 to 37 °C. Second, the soluble form of LLO (not bound to the cell membrane) irreversibly aggregates at neutral pH and 37 °C, thus limiting cytotoxic effects and abrogating the need to wash the cells. Finally, the degree of damage can be adjusted by varying the concentration of the toxin. However, a limitation of this assay is the temperature switch between 37 and 4 °C, which may affect the repair mechanism such as vesicular transport, endocytosis, and membrane fluidity, among other processes, which are influenced by temperature[52,53,54]. It is important to verify that any pharmacological inhibitor included in the assay does not interfere with the formation of LLO pores by performing a hemolysis assay in the presence (versus absence) of the drug[55]. Due to potential batch differences in LLO activity, it is important to prepare a stock of LLO that is large enough for an entire high-throughput screen[55].

We included the use of cells expressing the nuclear-localized Histone-2B-GFP chimera as a means to enumerate cells before and after the membrane repair assay via microscopic imaging followed by automated image analysis. Importantly, equivalent cell counts across conditions and unchanging cell counts before and after the kinetic assay are crucial as PI or CNABD fluorescence intensities cannot easily be normalized. Indeed, a difference in cell count will result in differences in the degree of damage by a given concentration of LLO, which cannot be corrected for via fluorescence normalization due to variations in resealing efficiency (**Figure 7**). We showed that Histone-2B-GFP expression does not interfere with PI or CNABD incorporation or fluorescence emission. Conversely, PI or CNABD incorporation does not affect GFP-based cell enumeration. If other combinations of fluorophores are to be used, it would be necessary to assess potential spectral overlap between fluorochromes, as was performed in this work. Although PI has been extensively used to measure membrane damage, we show that CNABD is an excellent substitute that exhibits higher fluorescence quantum yield, resulting in a larger dynamic range suitable for characterizing resealing efficiency.

Z-factor and SSMD confirmed that this assay has the robustness necessary to perform high-throughput analyses. The calculation of the resealing efficiency is a critical and reliable tool to identify potential hits. In addition, the mixed effects model can be used as a statistical tool to evaluate hits within a single assay. The experimental plan must include a minimum of three technical replicates if the screen can be repeated several times. Quadruplicates should be used if statistical tools, such as the mixed effects model, are to be included in a single experiment, whether or not it will be repeated. It is advised however to perform the screen several times and to validate the results by performing complementary experiments.

Disclosures

The authors have nothing to disclose.

Acknowledgements

We acknowledge Dr. Jesse Kwiek (The Ohio State University) for kindly allowing us to use his multi-mode detection platform for some preliminary experiments. Research reported in this article was supported by the National Institute of Allergy and Infectious Diseases of the National Institutes of Health under award number RO1AI107250 to Stephanie Seveau. The content is solely the responsibility of the authors and does not necessarily represent the official views of the National Institutes of Health.

References

1. Demonbreun, A.R., McNally, E.M. Plasma Membrane Repair in Health and Disease. *Current Topics in Membranes.* **77**, 67-96 (2016).
2. Howard, A.C., McNeil, A.K., McNeil, P.L. Promotion of plasma membrane repair by vitamin E. *Nature Communications.* **2**, 597 (2011).
3. Howard, A.C., et al. A novel cellular defect in diabetes: membrane repair failure. *Diabetes.* **60** (11), 3034-43 (2011).
4. Lozano, M.L., et al. Towards the targeted management of Chediak-Higashi syndrome. *Orphanet Journal of Rare Diseases.* **9**, 132 (2014).
5. Vainzof, M., et al. Dysferlin protein analysis in limb-girdle muscular dystrophies. *Journal of Molecular Neuroscience.* **17** (1), 71-80 (2001).
6. Huynh, C., et al. Defective lysosomal exocytosis and plasma membrane repair in Chediak-Higashi/beige cells. *Proceeding of the National Academy of Sciences of the United States of America.* **101** (48), 16795-800 (2004).
7. Cooper, S.T., McNeil, P.L. Membrane Repair: Mechanisms and Pathophysiology. *Physiological Reviews.* **95** (4), 1205-40 (2015).

8. Steinhardt, R.A., Bi G., J.M., Alderton J.M. Cell membrane resealing by a vesicular mechanism similar to neurotransmitter release. *Science.* **263** (5145), 390-3 (1994).
9. De Mello, W.C. Membrane sealing in frog skeletal-muscle fibers. *Proceedings of the National Academy of Sciences of the United States of America.* **70** (4), 982-4 (1973).
10. Fishman, H.M., Tewari K.P., Stein P.G. Injury-induced vesiculation and membrane redistribution in squid giant axon. *Biochimica et Biophysica Acta.* **1023** (3), 421-35 (1990).
11. Davenport, N.R., Bement, W.M. Cell repair: Revisiting the patch hypothesis. *Communicative & Integrative Biology.* **9** (6), e1253643 (2016).
12. McNeil, P.L., et al. Patching plasma membrane disruptions with cytoplasmic membrane. *Journal of Cell Science.* **113** (11), 1891-902 (2000).
13. Terasaki, M., Miyake, K., McNeil, P.L. Large plasma membrane disruptions are rapidly resealed by Ca2+-dependent vesicle-vesicle fusion events. *Journal of Cell Biology.* **139** (1), 63-74 (1997).
14. Bi, G.Q., Alderton, J.M., Steinhardt, R.A. Calcium-regulated exocytosis is required for cell membrane resealing. *Journal of Cell Biology.* **131** (6 Pt. 2), 1747-58 (1995).
15. Tam, C., et al. Exocytosis of acid sphingomyelinase by wounded cells promotes endocytosis and plasma membrane repair. *Journal of Cell Biology.* **189** (6), 1027-38 (2010).
16. Rodriguez, A., et al. Lysosomes behave as Ca2+-regulated exocytic vesicles in fibroblasts and epithelial cells. *Journal of Cell Biology.* **137** (1), 93-104 (1997).
17. Reddy, A., Caler, E.V., Andrews, N.W. Plasma membrane repair is mediated by Ca(2+)-regulated exocytosis of lysosomes. *Cell.* **106** (2), 157-69 (2001).
18. Jimenez, A.J., et al. ESCRT machinery is required for plasma membrane repair. *Science.* **343** (6174), 1247136 (2014).
19. Pathak-Sharma, S., et al. High-Throughput Microplate-Based Assay to Monitor Plasma Membrane Wounding and Repair. *Frontiers in Cellular and Infection Microbiology.* **7**, 305 (2017).
20. Hamon, M.A., et al. Listeriolysin O: the Swiss army knife of Listeria. *Trends in Microbiology.* **20** (8), 360-8 (2012).
21. Seveau, S., Multifaceted activity of listeriolysin O, the cholesterol-dependent cytolysin of Listeria monocytogenes. *Subcellular Biochemistry.* **80**, 161-95 (2014).
22. Osborne, S.E., Brumell, J.H., Listeriolysin O: from bazooka to Swiss army knife. *Philosophical Transactions of the Royal Society of London B: Biological Sciences.* **372** (1726), (2017).
23. Lukoyanova, N., Hoogenboom, B.W., Saibil, H.R. The membrane attack complex, perforin and cholesterol-dependent cytolysin superfamily of pore-forming proteins. *Journal of Cell Science.* **129** (11), 2125-33 (2016).
24. Tweten, R.K. Cholesterol-dependent cytolysins, a family of versatile pore-forming toxins. *Infection and Immunity.* **73** (10), 6199-209 (2005).
25. Koster, S., et al. Crystal structure of listeriolysin O reveals molecular details of oligomerization and pore formation. *Nature Communications.* **5**, 3690 (2014).
26. Duncan, J.L., Schlegel, R. Effect of streptolysin O on erythrocyte membranes, liposomes, and lipid dispersions. A protein-cholesterol interaction. *Journal of Cell Biology.* **67** (1), 160-74 (1975).
27. Morgan, P.J., et al. Subunit organisation and symmetry of pore-forming, oligomeric pneumolysin. *FEBS Letters.* **371** (1), 77-80 (1995).
28. Leung, C., et al. Stepwise visualization of membrane pore formation by suilysin, a bacterial cholesterol-dependent cytolysin. *eLife.* **3**, e04247 (2014).
29. Marchioretto, M., et al. What planar lipid membranes tell us about the pore-forming activity of cholesterol-dependent cytolysins. *Biophysical Chemistry.* **182**, 64-70 (2013).
30. Palmer, M., et al. Assembly mechanism of the oligomeric streptolysin O pore: the early membrane lesion is lined by a free edge of the lipid membrane and is extended gradually during oligomerization. *European Molecular Biology Organization Journal.* **17** (6), 1598-605 (1998).
31. Bavdek, A., et al. pH dependence of listeriolysin O aggregation and pore-forming ability. *Federation of European Biochemical Society Journal.* **279** (1), 126-41 (2012).
32. Schuerch, D.W., Wilson-Kubalek, E.M., Tweten, R.K. Molecular basis of listeriolysin O pH dependence. *Proceeding of the National Academy of Sciences of the United States of America.* **102** (35), 12537-42 (2005).
33. Cassidy, S.K., O'Riordan, M.X. More than a pore: the cellular response to cholesterol-dependent cytolysins. *Toxins (Basel.).* **5** (4), 618-36 (2013).
34. Lam, J., et al. Host cell perforation by listeriolysin O (LLO) activates a Ca(2+)-dependent cPKC/Rac1/Arp2/3 signaling pathway that promotes L. monocytogenes internalization independently of membrane resealing. *Molecular Biology of the Cell.* (2017).
35. Gekara, N.O., Weiss, S. Lipid rafts clustering and signalling by listeriolysin O. *Biochemical Society Transactions.* **32** (Pt 5), 712-4 (2004).
36. Magassa, N., Chandrasekaran, S., Caparon, M.G. Streptococcus pyogenes cytolysin-mediated translocation does not require pore formation by streptolysin O. *European Molecular Biology Organization Reports.* **11** (5), 400-5 (2010).
37. Baba, H., et al. Induction of gamma interferon and nitric oxide by truncated pneumolysin that lacks pore-forming activity. *Infection and Immunity.* **70** (1), 107-13 (2002).
38. Carrero, J.A., Vivanco-Cid, H., Unanue, E.R. Listeriolysin o is strongly immunogenic independently of its cytotoxic activity. *Public Library of Science One.* **7** (3), e32310 (2012).
39. Coconnier, M.H., et al. Listeriolysin O-induced stimulation of mucin exocytosis in polarized intestinal mucin-secreting cells: evidence for toxin recognition of membrane-associated lipids and subsequent toxin internalization through caveolae. *Cell Microbiology.* **2** (6), 487-504 (2000).
40. Suzuki, T., et al. DNA staining for fluorescence and laser confocal microscopy. *Journal of Histochemistry and Cytochemistry.* **45** (1), 49-53 (1997).
41. Bink, K., et al. TO-PRO-3 is an optimal fluorescent dye for nuclear counterstaining in dual-colour FISH on paraffin sections. *Histochemistry and Cell Biology.* **115** (4), 293-9 (2001).
42. Zhang, J.H., Chung, T.D., Oldenburg, K.R. A Simple Statistical Parameter for Use in Evaluation and Validation of High Throughput Screening Assays. *Journal of Biomolecular Screening.* **4** (2), 67-73 (1999).
43. Birmingham, A., et al. Statistical methods for analysis of high-throughput RNA interference screens. *Nature Methods.* **6** (8), 569-75 (2009).
44. Zhang, X.D. A pair of new statistical parameters for quality control in RNA interference high-throughput screening assays. *Genomics.* **89** (4), 552-61 (2007).
45. Zhang, X.D. A new method with flexible and balanced control of false negatives and false positives for hit selection in RNA interference high-throughput screening assays. *Journal of Biomolecular Screening.* **12** (5), 645-55 (2007).
46. Idone, V., et al. Repair of injured plasma membrane by rapid Ca2+-dependent endocytosis. *Journal of Cell Biology.* **180** (5), 905-14 (2008).
47. Davenport, N.R., et al. Membrane dynamics during cellular wound repair. *Molecular Biology of the Cell.* **27** (14), 2272-85 (2016).

48. Defour, A., Sreetama, S.C., Jaiswal, J.K. Imaging cell membrane injury and subcellular processes involved in repair. *Journal of Visualized Experiments.* (85), (2014).
49. Lee, J.J.A., et al. Cell Membrane Repair Assay Using a Two-photon Laser Microscope. *Journal of Visualized Experiments.* (131), (2018).
50. Weisleder, N., et al. Visualization of MG53-mediated cell membrane repair using in vivo and in vitro systems. *Journal of Visualized Experiments.* (52), (2011).
51. Corrotte, M., et al. Toxin pores endocytosed during plasma membrane repair traffic into the lumen of MVBs for degradation. *Traffic.* **13** (3), 483-94 (2012).
52. Kuismanen, E., Saraste, J. Low temperature-induced transport blocks as tools to manipulate membrane traffic. *Methods in Cell Biology.* **32**, 257-74 (1989).
53. Togo, T., et al. The mechanism of facilitated cell membrane resealing. *Journal of Cell Science.* **112** (Pt 5), 719-31 (1999).
54. Johnson, S.A., et al. Temperature-dependent phase behavior and protein partitioning in giant plasma membrane vesicles. *Biochimica et Biophysica Acta.* **1798** (7), 1427-35 (2010).
55. Lam, J.G.T., et al. Host cell perforation by listeriolysin O (LLO) activates a Ca(2+)-dependent cPKC/Rac1/Arp2/3 signaling pathway that promotes Listeria monocytogenes internalization independently of membrane resealing. *Molecular Biology of the Cell.* **29** (3), 270-284 (2018).

